

Dynamically Stable Vortices in Exciton-Polariton Condensates Engineered by Repulsive Interactions

P. Raman,¹ R. Radha¹, Pankaj K. Mishra² and Paulsamy Muruganandam^{3,4}

¹*Centre for Nonlinear Science (CeNSc), Department of Physics,*

Government College for Women (A), Kumbakonam 612001, Tamil Nadu, India

²*Department of Physics, Indian Institute of Technology Guwahati 781039, Assam, India*

³*Department of Physics, Tamil Nadu, Bharathidasan University, Tiruchirappalli 620024, India*

⁴*Department of Medical Physics, Bharathidasan University, Tiruchirappalli 620024, Tamil Nadu, India*

(Dated:)

We present an analytical and numerical study of the dynamics and stability of exciton-polariton condensates described by the open-dissipative Gross-Pitaevskii equation, incorporating both binary and short-range three-body interactions. Using an asymptotic description, we identify the parameter regime and derive equations for the instability amplitude, providing insights into vortex formation via the snake instability of dark solitons. We find that a repulsive three-body interaction, when combined with a binary interaction, supports stable vortex-antivortex pair formation. On the other hand, the reinforcement of attractive three-body interactions with binary interaction triggers the emergence of snake instability, leading to boundary-driven vortex disintegration. The time evolution of the instability under the influence of reservoir effects indicates that the boundary effects are more pronounced, to the extent of destabilizing the vortices with attractive three-body interactions compared to repulsive three-body interactions, thereby underscoring the stable nature of vortices in the repulsive domain.

I. INTRODUCTION

Exciton-polariton condensates, which arise from the strong coupling between photons and excitons in semiconductor microcavities, represent a significant paradigm shift in the study of quantum fluids of light and matter [1–5]. Owing to their hybrid light–matter nature, polaritons inherit an exceptionally small effective mass from their photonic component [4, 6], enabling Bose-Einstein condensation at relatively high temperatures [1, 7], including room temperature in state-of-the-art perovskite-based microstructures [6, 8]. This makes them a versatile platform for exploring macroscopic quantum phenomena beyond the constraints of ultracold atomic gases [4, 9]. However, exciton-polariton condensates are short-lived, and stabilizing them continues to be an arduous task even today [3, 10].

A defining feature of exciton-polariton condensates is their intrinsically nonequilibrium character [3, 11]. Unlike equilibrium atomic Bose-Einstein condensates, polariton condensates are sustained by continuous optical pumping and are subject to rapid radiative decay [9, 12, 13]. Despite this driven-dissipative character, they exhibit the hallmark of quantum degeneracy, including superfluidity, long-range order, and the formation of quantized vortices [13–15]. The interplay of nonlinearity, gain, and loss in these systems leads to a rich landscape of phenomena, such as pattern formation, spontaneous symmetry breaking, and topological excitations [16, 17].

This unique non-equilibrium physics has stimulated extensive experimental and theoretical research, leading to the development of polariton lasers [18], ultrafast optical switches [19], and robust nonlinear excitations such as dark solitons and vortices [20–22]. Increasing attention has also been directed toward many-body correlation

effects, including the formation of composite polaronic quasiparticles mediated by biexciton and triexciton resonances [23]. To date, however, the dominant theoretical treatment of interactions in polariton condensates has been largely restricted to effective two-body processes, resulting in cubic nonlinearities within the mean-field description.

A natural, yet comparatively unexplored, extension of this framework involves higher-order interactions. In particular, effective three-body interactions may emerge from virtual excitation processes and can significantly modify a condensate’s stability and ground-state phase structure [24, 25]. While such interactions have been studied extensively in equilibrium atomic Bose-Einstein condensates (BECs), where they are known to stabilize quantum droplets and suppress collapse [26–28], their implications in non-equilibrium polariton systems remain largely unexplored. The specific role of three-body interactions in stabilizing topological excitations, such as quantized vortices and solitons, against dissipation and driving in polariton condensates constitutes a significant gap in the literature. In this paper we aim to address this gap by systematically investigating the impact of three-body interactions on the stability and dynamics of topological defects in exciton-polariton condensates.

In this work, we theoretically investigate the impact of two- and three-body interactions on the stability and dynamics of topological excitations in exciton-polariton condensates. Using the open-dissipative Gross-Pitaevskii equation and an asymptotic description, we elucidate how three-body interactions modulate the snake instability of dark solitons and the subsequent formation of vortex arrays. We demonstrate that repulsive three-body interactions can stabilize these excitations, while attractive interactions accelerate their decay, providing

new pathways to control quantum phenomena in driven-dissipative systems.

The paper is organized as follows. In Sec. II, we introduce the mean-field theoretical framework for the system and discuss the steady-state solutions under uniform continuous pumping. This section also focuses on the analysis of dark solitons in two dimensions, where we present the dark soliton solution and provide a hydrodynamic interpretation of the associated dynamics. The effects of weak and strong pumping are examined within appropriate approximations in the same section. Section III presents an asymptotic description that elucidates the behavior of two-dimensional dark solitons. In Sec. IV, we present numerical results based on the Gross-Pitaevskii mean-field model, focusing on the role of repulsive and attractive three-body interactions in vortex stability and dynamics. Finally, the main results are summarized, and perspectives for future work are discussed in Sec. V.

II. THE MEAN-FIELD MODEL

The dynamics of an exciton-polariton condensate within the mean-field framework is described by a coupled driven-dissipative system, comprising the Gross-Pitaevskii (GP) equation for the condensate wavefunction and a rate equation for the exciton reservoir of the following form [10, 22]:

$$i\frac{\partial\Psi}{\partial t} = \left[-\frac{\hbar^2}{2m}\nabla^2 + U(\vec{r}, t) + \frac{i\hbar}{2}(Rn_R - \gamma_C) \right] \Psi, \quad (1a)$$

$$\frac{\partial n_R}{\partial t} = P(\vec{r}, t) - (\gamma_R + R|\Psi|^2)n_R. \quad (1b)$$

Here, the effective potential is given by $U(\vec{r}, t) = g_c|\Psi|^2 + \chi_c|\Psi|^4 + g_R n_R$. The g_C denotes the strength of two-body nonlinear interactions, χ_c represents the strength of three-body interactions, and g_R accounts for the interaction between the reservoir and the polariton condensate. The parameter R corresponds to the stimulated scattering rate, γ_C is the loss rate of the condensate polariton, and γ_R denotes the decay rate of the exciton reservoir given by Eq. (1b). High-energy exciton-like particles are injected into the reservoir by laser pump $P(\vec{r}, t)$. Under continuous wave and spatially uniform pumping, where $P(\vec{r}, t) = P_0 = \text{constant}$, the steady-state solution is given by

$$\Psi(\vec{r}, t) = \Psi_0 = \sqrt{n_C^0} e^{-i(E_0/\hbar)t}, \quad n_R(\vec{r}, t) = n_R^0. \quad (2)$$

where, n_C^0 and n_R^0 denote the steady state densities corresponding to the condensate polariton and reservoir, respectively. In the weak pumping limit, the condensate density vanishes, i.e. $n_C^0 = 0$, while the reservoir density reaches a steady state density $n_R^0 = P_0/\gamma_R$ with the balance gain and loss at the threshold pump power. When the pumping exceeds this threshold as defined by Eq. (2), the condensate density becomes non-zero, i.e., n_C^0 , and

a macroscopic condensate emerges. Above threshold, the steady-state homogeneous densities of the condensate and reservoir are given by:

$$n_C^0 = (P_0 - P_{th})/\gamma_C, \quad n_R^0 = n_R^{th} = \gamma_C/R, \quad (3)$$

The model can be written in dimensionless form by scaling the unit of healing length $r_h = \hbar/(Mc_s)$ and time as $\tau_0 = r_h/c_s$. Here, $c_s = (g_C n_C^*/M)^{1/2}$ is a local sound velocity in the condensate and n_C^* is the characteristic density of the condensate. In dimensionless form, the wavefunction $\bar{\Psi} = \Psi/\sqrt{n_C^*}$ and the reservoir density is given by $\bar{n}_R = n_R/n_C^*$. Under these circumstances, Eq. (1) becomes,

$$i\frac{\partial\bar{\Psi}}{\partial t} = -\frac{1}{2}\nabla^2\bar{\Psi} + \bar{U}(\vec{r}, t) + \frac{i}{2}(\bar{R}n_R - \bar{\gamma}_C)\bar{\Psi}, \quad (4a)$$

$$\frac{\partial\bar{n}_R}{\partial t} = \bar{P} - (\bar{\gamma}_R n_R + \bar{R}|\bar{\Psi}|^2 n_R). \quad (4b)$$

Here, $\bar{U}(\vec{r}, t) = |\bar{\Psi}|^2 + \bar{\chi}_c|\bar{\Psi}|^4 + \bar{g}_R\bar{n}_R + \bar{g}_R\bar{n}_R^2$. The other dimensionless parameters are

$$\bar{\chi} = \frac{\chi}{g_C}, \quad \bar{g}_R = \frac{g_R}{g_C}, \quad \bar{\gamma}_C = \frac{\hbar\gamma_C}{g_C n_C^*}, \quad \bar{R} = \frac{\hbar R}{g_C}$$

For continuous background density, the characteristic value of the condensate density is given by $n_C^* = n_C^0$. Using this relation, the homogeneous steady state solution can be represented as [22]

$$\bar{\Psi}_0 = \exp(-i\bar{\omega}t), \quad \bar{\omega} = \bar{g}_R n_R^{th}(1 + n_R^{th}). \quad (5)$$

Let's consider the perturbations of the condensate wavefunction and the reservoir density in the general form as [29]

$$\bar{\Psi} = \bar{\Psi}_0(t)\psi(\vec{r}, t), \quad \bar{n}_R = \bar{n}_R^{th} + m_R(\vec{r}, t). \quad (6)$$

When we substitute the above in Eqs. (4a) and (4b), we obtain

$$i\frac{\partial\psi}{\partial t} = \left[-\frac{1}{2}\nabla^2 - (1 - |\psi|^2) - \chi(1 - |\psi|^4) + \bar{g}_R m_R + \bar{g}_R m_R^2 + \frac{i}{2}\bar{R}m_R \right] \psi, \quad (7a)$$

$$\frac{\partial m_R}{\partial t} = \bar{\gamma}_C(1 - |\psi|^2) - \bar{\gamma}_R m_R - \bar{R}|\psi|^2 m_R, \quad (7b)$$

where $\bar{\gamma}_R = \bar{R}/(P_0/P_{th} - 1)$.

The coupled Eqs. (7a) and (7b) describe the driven-dissipative dynamics of the condensate wavefunction and the reservoir density in the presence of nonlinear interactions, gain, and loss. To gain insight into the fundamental behavior of the system, it is useful to first analyze the stationary solutions that arise from the balance between pumping and dissipation. In particular, we consider the case of spatially uniform and time-independent pumping, for which the system can support a homogeneous nonequilibrium steady state. The properties of this steady state form the basis for understanding the subsequent dynamical behavior of the condensate.

A. Steady-state under uniform continuous pumping

The driven-dissipative nature of the condensate allows the system to reach a nonequilibrium steady state determined by the balance between gain and loss. To characterize this state, we consider the case of spatially uniform and continuous pumping and determine the corresponding homogeneous stationary solutions. Under spatially uniform and time-independent pumping $P(\vec{r}, t) = P_0$, the system supports homogeneous stationary solutions of the form

$$\Psi(\vec{r}, t) = \sqrt{n_C^0} e^{-i\mu t}, \quad n_R(\vec{r}, t) = n_R^0, \quad (8)$$

where $|\Psi_0|^2 = n_C^0$ is real, n_R^0 is constant, and μ is the dimensionless chemical potential.

Substituting (8) into the dimensionless equations (4) yields the following algebraic conditions

$$\mu\Psi_0 = (\Psi_0^2 + g_R n_R^0)\Psi_0 + \frac{i}{2}(Rn_R^0 - \gamma_C)\Psi_0, \quad (9a)$$

$$0 = P_0 - (\gamma_R + R\Psi_0^2)n_R^0. \quad (9b)$$

For a non-vanishing condensate amplitude $\Psi_0 > 0$, the imaginary part of the first equation requires the gain-loss balance

$$n_R^0 = \frac{\gamma_C}{R}. \quad (10)$$

This clamping of the reservoir density above threshold is a hallmark of polariton condensation [3, 9, 30].

Inserting the clamped value into the second (reservoir) equation determines the condensate density:

$$\Psi_0^2 = \frac{P_0 - P_{\text{th}}}{\gamma_C}, \quad P_{\text{th}} \equiv \frac{\gamma_C \gamma_R}{R}, \quad (11)$$

where P_{th} is the dimensionless threshold pump intensity. The real part of the wave-function equation then gives the chemical potential

$$\mu = \Psi_0^2 + g_R \frac{\gamma_C}{R}. \quad (12)$$

Below threshold ($P_0 < P_{\text{th}}$), the only physical solution is the empty state $\Psi_0 = 0$, in which case the reservoir density reduces to the linearly pumped value $n_R^0 = P_0/\gamma_R$ and the chemical potential (formally obtained by taking the zero-density limit) is $\mu = g_R P_0/\gamma_R$.

The complete steady-state solution above threshold therefore reads

$$\Psi_0 = \sqrt{\frac{P_0 - P_{\text{th}}}{\gamma_C}}, \quad n_R^0 = \frac{\gamma_C}{R}, \quad \mu = \frac{P_0 - P_{\text{th}}}{\gamma_C} + \frac{g_R \gamma_C}{R}. \quad (13)$$

Above threshold, the reservoir density is pinned at a constant value independent of pumping strength, while the condensate density increases linearly with the excess

pump intensity $P_0 - P_{\text{th}}$. This nonlinear threshold behavior and reservoir clamping are routinely observed in experiments [30, 31] and constitute the defining signature of Bose-Einstein condensation in driven-dissipative polariton systems.

B. Hydrodynamic Interpretation of the Snake Instability

An intuitive understanding of the snake instability can be gained within the hydrodynamic representation of the driven-dissipative Gross-Pitaevskii equation. Using the Madelung transformation

$$\Psi(\vec{r}, t) = \sqrt{n_C^0} e^{iS(\vec{r}, t)}, \quad (14)$$

the superfluid density $n_C^0 = n(x, y) = |\Psi|^2$ and velocity field $\vec{v}(\vec{r}, t) = \frac{\hbar}{M} \nabla S(\vec{r}, t)$ obey continuity and Euler-type equations modified by gain, loss, and reservoir-mediated interactions [9, 12, 32]. The current density of the wavefunction can be written as

$$\vec{j}(\vec{r}, t) = \left(\frac{\hbar}{2Mi} \right) [\Psi^* \nabla \Psi - (\nabla \Psi^*) \Psi]. \quad (15)$$

The current density takes the hydrodynamic form as

$$\vec{j}(\vec{r}, t) = n(\vec{r}, t) v(\vec{r}, t). \quad (16)$$

Here, the rotational velocity $v(\vec{r}, t)$ can be expressed in terms of velocity potential $\Phi(\vec{r}, t)$

$$\vec{v}(\vec{r}, t) = \nabla \Phi(\vec{r}, t), \quad (17)$$

where the velocity potential is

$$\Phi(\vec{r}, t) = \frac{\hbar}{M} S(\vec{r}, t). \quad (18)$$

Taking the gradient on both sides of Eq. (18), we have

$$\nabla \Phi(\vec{r}, t) = \frac{\hbar}{M} \nabla S(\vec{r}, t), \quad (19)$$

which implies

$$\mathbf{v}(\vec{r}, t) = \frac{\hbar}{M} \nabla S(\vec{r}, t). \quad (20)$$

Using the Madelung transformation of the condensate wavefunction, the velocity field can equivalently be written as

$$\mathbf{v}(\vec{r}, t) = \frac{\hbar}{M} \nabla S(\vec{r}, t) = \frac{\hbar}{M} \frac{\text{Im}(\Psi^* \nabla \Psi)}{|\Psi|^2}. \quad (21)$$

Assuming a uniform background density $n(x, y) = n_0$, the wavefunction is given by

$$\Psi(x, y, t) = \sqrt{n_0} \left[\tanh\left(\frac{x}{\xi_s}\right) + iA(t) \frac{\sin(ky)}{\cosh(x/\xi_s)} \right], \quad (22)$$

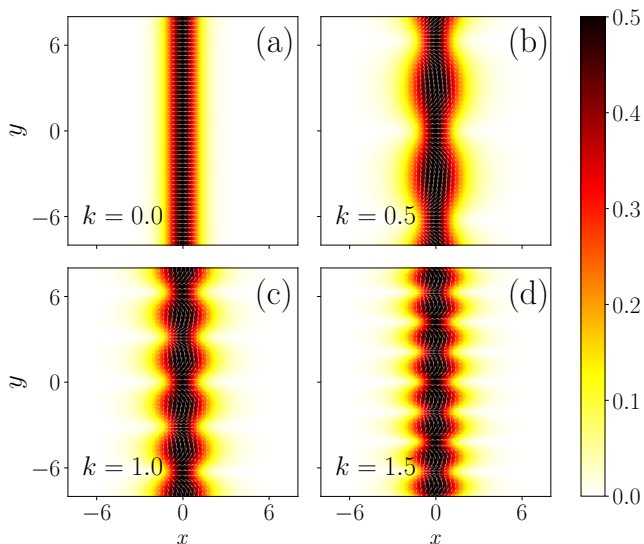


FIG. 1. The velocity fields from Eq. (23) for an instability amplitude $A(0) = 0.25$ for different k .

The velocity components v_x and v_y [See Appendix A for details] are given by

$$v_x = -A(t) \operatorname{sech}^3\left(\frac{x}{\xi}\right) \sin(ky) - \tanh^2\left(\frac{x}{\xi}\right) \operatorname{sech}\left(\frac{x}{\xi}\right) \sin(ky), \quad (23a)$$

$$v_y = -A(t) \tanh\left(\frac{x}{\xi}\right) \operatorname{sech}\left(\frac{x}{\xi}\right) \cos(ky). \quad (23b)$$

These expressions show that the transverse modulation of the soliton introduces spatially varying velocity components along both the longitudinal (x) and transverse (y) directions. In particular, the dependence of $\sin(ky)$ and $\cos(ky)$ indicate that the velocity field develops periodic variations along the soliton line. As the instability amplitude $A(t)$ grows, these transverse velocity perturbations become increasingly pronounced, leading to bending and deformation of the initially straight soliton.

Figure 1 illustrates the velocity fields for different wave numbers (k) at a fixed instability amplitude $A = 0.25$. With increasing k , the spatial modulation of the velocity field becomes stronger, resulting in enhanced transverse flows around the soliton core. From a hydrodynamic perspective, these growing transverse flows signal the breakdown of the planar soliton structure and the onset of the snake instability. Consequently, the soliton becomes dynamically unstable and eventually decays into pairs of vortices, which correspond to localized phase singularities in the condensate. From a hydrodynamic viewpoint, this growing transverse circulation signals the onset of the snake instability, where the planar soliton becomes dynamically unstable to transverse perturbations. As the instability develops further, the soliton stripe breaks up and nucleates vortex–antivortex pairs, which appear as

localized phase singularities in the condensate and represent the final stage of the snake instability.

III. ASYMPTOTIC DESCRIPTION OF THE DYNAMICS OF THE TWO-DIMENSIONAL DARK SOLITON

Several experimental and theoretical methods exist for generating and studying vortices in BECs [17, 32–35]. These include phase imprinting, rotating traps, stirring with laser beams, and dynamical instabilities of nonlinear excitations. Among these mechanisms, the decay of a dark soliton via the transverse (snake) instability provides a particularly direct route for vortex nucleation in effectively two-dimensional geometries. This process is not only experimentally accessible but also theoretically appealing, as it connects soliton physics to vortex dynamics through a well-defined instability mechanism. In one spatial dimension, dark solitons are robust nonlinear excitations characterized by a localized density depletion and phase jump across the nodal plane. However, in two dimensions, such planar structures are dynamically unstable against transverse perturbations. Small modulations along the direction perpendicular to propagation grow exponentially, leading to the breakup of the soliton stripe into vortex–antivortex pairs. This instability mechanism, commonly referred to as the snake instability, plays a central role in the formation of coherent vortex structures from initially non-topological excitations.

To capture the early stages of this dynamics and the subsequent evolution of the soliton filament, it is useful to develop an asymptotic description valid in the regime where the soliton width is small compared to the characteristic length scale of the background inhomogeneity [17]. In this framework, the dark soliton is treated as a quasi-one-dimensional object embedded in a slowly varying two-dimensional condensate background. The separation of scales between the soliton core (of order of the healing length) and the external trapping potential allows for a systematic reduction of the Gross–Pitaevskii equation to an effective equation governing the soliton centerline dynamics.

In the asymptotic description, the wavefunction of a two-dimensional dark soliton in an inhomogeneous system can be written as

$$\psi(\vec{r}, t) = G(\vec{r})F(\vec{r}, t), \quad (24)$$

where $G(\vec{r})$ represents the solution of the unperturbed condensate under the influence of the external potential $U(\vec{r})$, while $F(\vec{r}, t)$ describes the time evolution of finite-amplitude perturbations on an initially inhomogeneous condensate. In the absence of the reservoir density perturbation, Eq. (7a) reduces to a nonlinear Schrödinger equation of the following form

$$i\frac{\partial\psi}{\partial t} + \frac{1}{2}\nabla^2\psi + (1 - |\psi|^2)\psi + \chi_c(1 - |\psi|^4)\psi = 0 \quad (25)$$

which admits dark soliton solution in the form of Eq.(22). Substituting the ansatz (24) into (25), we obtain a set of coupled equations for the unperturbed and perturbed components [36],

$$\frac{1}{2}\nabla^2 G + \chi_c (1 - |G|^2)G - (1 - |G|^4)G = 0 \quad (26)$$

$$i\frac{\partial F}{\partial t} + \frac{\nabla^2 F}{2} + |G|^2 (1 - |F|^2)F + \chi_c |G|^4 (1 - |F|^4)F = -\frac{1}{G}\nabla G \cdot \nabla F \quad (27)$$

Assuming that the unperturbed component $G(\vec{r})$ and the external potential $U(\vec{r}, t)$ vary slowly within the localization region, the dynamics of the two-dimensional quasi-soliton in a condensate at rest can be described by

$$G(\vec{r}) = g(\vec{r}) \exp(i\theta) \quad (28)$$

where θ is a constant condensate phase and $g(\mathbf{r})$ is a real-valued function of the position. The position vector is $\vec{r} = x\hat{x} + y\hat{y}$, with \hat{x} and \hat{y} denoting the cartesian unit vectors. To describe the soliton geometry more conveniently, we transform from Cartesian coordinates to orthogonal curvilinear coordinates (s, η) as

$$\vec{r} = \vec{r}_0(s) + \eta \vec{n}_0(s) \quad (29)$$

where, $\vec{r}_0(s)$ specifies the centre of the dark soliton and $\vec{n}_0(s)$ is the local normal vector. In these coordinates, the condensate equation can be reformulated in a natural way for analyzing the soliton dynamics. Now, the condensate equation in the orthogonal curvilinear coordinates can be written as

$$i\frac{\partial F}{\partial t} + \frac{1}{2h_s h_\eta} \left[\frac{\partial}{\partial s} \left(\frac{h_\eta}{h_s} \frac{\partial F}{\partial s} \right) + \frac{\partial}{\partial \eta} \left(\frac{h_s}{h_\eta} \frac{\partial F}{\partial \eta} \right) \right] + |G|^2 (1 - |F|^2)F + \chi_c |G|^4 (1 - |F|^4)F = \frac{1}{G} \left[\frac{1}{h_s^2} \frac{\partial G}{\partial s} \frac{\partial F}{\partial s} + \frac{1}{h_\eta^2} \frac{\partial G}{\partial \eta} \frac{\partial F}{\partial \eta} \right] \quad (30)$$

We expand the undisturbed function $|G(\mathbf{r})|^2$ near the curve $r_0(s)$ in the form of a Taylor series in terms of η as

$$|G(\vec{r})|^2 = |G(\vec{r}_0 + \eta \vec{n}_0)|^2 \quad (31)$$

Upon expanding the $|G(\vec{r})|$ at $\eta = 0$, we obtain

$$|G(\vec{r})|^2 = |G_0|^2 + \eta \left. \frac{\partial |G|^2}{\partial \eta} \right|_{\eta=0} + \frac{\eta^2}{2} \left. \frac{\partial^2 |G|^2}{\partial \eta^2} \right|_{\eta=0} \quad (32)$$

The transformed equation can be written as

$$i\frac{\partial F}{\partial t} + \frac{1}{2}\frac{\partial^2 F}{\partial s^2} + \frac{1}{2}\frac{\partial^2 F}{\partial \eta^2} + |G(r_0)|^2(1 - |F|^2)F + \chi_c |G(r_0)|^4(1 - |F|^4)F = -\frac{\kappa \eta}{2} \frac{\partial^2 F}{\partial s^2} + \frac{\kappa}{2} \frac{\partial^2 F}{\partial \eta^2} - \left[\frac{\partial |G|^2}{\partial \eta} \right]_{\eta=0} \eta(1 - |F|^2)F - \chi_c \left[\frac{\partial |G|^4}{\partial \eta} \right]_{\eta=0} \eta(1 - |F|^4)F - \left[\frac{1}{G} \frac{\partial G}{\partial s} \right] \Big|_{\eta=0} \frac{\partial F}{\partial s} - \left[\frac{1}{G} \frac{\partial G}{\partial \eta} \right] \Big|_{\eta=0} \frac{\partial F}{\partial \eta} + \mathcal{O}(\lambda^2) \quad (33)$$

After this transformation, the solution of Eq.(33) near the curve $r_0(s)$ can be represented as an asymptotic series of λ , with the instability amplitude slowly varying in time given by $A(t) = A(\lambda t)$ where $\lambda \ll 1$. Under these circumstances, the solutions can be expressed in the form of asymptotic expansion in λ with $\xi = x/\xi_s$ as

$$\psi(\vec{r}, t) = \psi_s(\xi, y, A(\lambda t)) + \sum_{j=1}^{\infty} \lambda^j \psi_s(\xi, y, A(\lambda t)) \quad (34a)$$

$$m_R(\vec{r}, t) = \lambda m_R^0(\xi, y, \lambda t) + \sum_{j=1}^{\infty} \lambda^{j+1} m_{Rj}(\xi, y, \lambda t) \quad (34b)$$

We now substitute Eq.(34a) into (7a) and consider only the terms upto the first order in λ , the linear inhomogeneous equation $\psi_1(\xi, y, \lambda t)$ takes the form as

$$\frac{1}{2}\frac{\partial^2}{\partial \xi^2} + \frac{1}{2}\frac{\partial^2}{\partial y^2} - [(1 - 2|\psi_s|^2) + \chi((1 - 3|\psi_s|^4))] + [1 + 2\chi|\psi_s|^2]\psi_s^2 \psi_1^* = i\frac{\partial A}{\partial t} + \frac{\partial \psi_s}{\partial A} - \mathcal{R}(m_R^0, \psi_s) \quad (35)$$

From this, the Fredholm alternative can be defined as

$$\text{Re} \left[\int_{-\infty}^{\infty} \left(i\frac{\partial A}{\partial t} + \frac{\partial \psi_s}{\partial A} - \mathcal{R}(m_R^0, \psi_s) \frac{\partial \psi_s^*}{\partial \xi} \right) d\xi \right] = 0 \quad (36)$$

Eq.(36) leads to the dynamical equation of the following form

$$\frac{d\mathcal{E}_s}{dt} = \int_{-\infty}^{+\infty} d\xi dy \left(\mathcal{R}(m_R^0, \psi_s) \frac{\partial \psi_s^*}{\partial \xi} + \mathcal{R}^*(m_R^0, \psi_s) \frac{\partial \psi_s}{\partial \xi} \right) \quad (37)$$

The energy of the dark soliton will now become

$$\mathcal{E}_s = \int d\xi dy \left[\frac{1}{2} |\nabla \psi|^2 + \frac{1}{2} (1 - |\psi|^2)^2 + \frac{\chi}{3} (1 - |\psi|^2)^3 \right] \quad (38)$$

$$\begin{aligned} \mathcal{E}_s = A^2 & \left(\frac{k^2 \xi}{2} - \frac{8\xi\chi}{15} - \frac{2\xi}{3} + \frac{1}{6\xi} \right) - \frac{1}{9}\xi\chi A^6 \\ & + A(t)^4 \left(\frac{2\xi\chi}{5} + \frac{\xi}{4} \right) + \frac{16\xi\chi}{45} + \frac{2\xi}{3} + \frac{2}{3\xi} \end{aligned} \quad (39)$$

Since the instability amplitude $A(t)$ is very small, we can neglect the higher order powers of instability amplitude to obtain stable vortex solutions as

$$\mathcal{E}_s = A^2 \left(\frac{k^2 \xi}{2} - \frac{8\xi\chi}{15} - \frac{2\xi}{3} \right) + \frac{16\xi\chi}{45} + \frac{2\xi}{3} + \frac{2}{3\xi} \quad (40)$$

A. Weak-pumping region

In order to understand the influence of the reservoir on the transverse instability of the dark soliton, we now analyze the dynamics in the weak-pumping regime. Physically, this regime corresponds to pumping strengths slightly above the condensation threshold, where the reservoir density remains small, and its response to condensate fluctuations can be treated perturbatively. This condition can be expressed as

$$\frac{P_0}{P_{\text{th}}} - 1 \ll 1. \quad (41)$$

In this limit, the relaxation rate of the reservoir is typically much larger than the characteristic timescale of the condensate dynamics. As a result, the reservoir adjusts rapidly to variations in the condensate density and can be treated within an adiabatic approximation. Consequently, the spatial scale of the reservoir perturbation $m_R^0(\xi, y, \lambda t)$ becomes comparable to the width of the dark soliton, ξ_s .

From the reservoir rate equation (7b) together with the asymptotic expansion (34b), the leading-order reservoir perturbation is directly coupled to the condensate density $|\psi_s(\xi, y, \lambda t)|^2$. In the weak-pumping limit, the ratio of the condensate decay rate to the reservoir relaxation rate is small,

$$\frac{\gamma_C}{\gamma_R} \ll 1,$$

leading to the the small parameter

$$\lambda = \frac{\gamma_C}{\gamma_R} \ll 1.$$

The leading order contribution to the reservoir density perturbation is therefore given by

$$m_R^0 = \frac{\gamma_C}{\gamma_R} (1 - |\psi_s|^2). \quad (42)$$

where the dark soliton ansatz is defined in transformed coordinates with background density n as

$$\psi_s(\xi, y, t) = \sqrt{n} \left[\tanh(\xi) + iA(t) \frac{\sin(ky)}{\cosh(\xi)} \right] \quad (43)$$

Substituting Eq. (42) into the dynamical equation (37) and using the dark-soliton ansatz $\psi_s(\xi, y, t)$ defined above, we obtain the evolution equation for the instability amplitude $A(t)$,

$$\dot{A} = \alpha A^2, \quad (44)$$

where

$$\alpha = \frac{\sqrt{n}\pi^2 R \xi_s \gamma_C}{\gamma_R} \left(1 - \frac{n}{2} \right).$$

The solution of the above ordinary differential equation (44) can be written as

$$A(t) = \frac{A_0}{1 - \alpha A_0 t} \quad (45)$$

To find the disappearance/lifetime of the stable vortices, we need to have

$$1 - \alpha A_0 t = 0 \quad (46)$$

From this, we can obtain the lifetime τ of the vortices as:

$$\tau = \frac{1}{\alpha A_0} \quad (47)$$

From this equation, the disappearance of the stable vortices is determined by

$$\frac{1}{\tau} = \frac{1}{2} \left(n - \frac{n^3}{2} \right) \left(\frac{A_0 \pi^2 R \xi_s \gamma_C}{\gamma_R} \right) \quad (48)$$

The disappearance of the stable vortex is determined by the lifetime (τ) of the dark soliton as

$$\tau = \frac{2\tau_0}{A_0 \pi^2 (n - \frac{n^3}{2}) \gamma_C} \left(\frac{P_{\text{th}}}{P_0 - P_{\text{th}}} \right) \quad (49)$$

The above analysis shows that in the weak-pumping regime, the reservoir responds adiabatically to the condensate density, and the transverse instability of the dark soliton is governed by the nonlinear evolution equation for the instability amplitude $A(t)$. The resulting growth of the perturbation determines the lifetime of the vortices formed through the snake instability, which depends explicitly on the ratio γ_C/γ_R and the pumping strength relative to the threshold. In this regime, the dynamics are dominated by the fast relaxation of the reservoir, leading to a relatively simple relation between the instability growth and the condensate parameters.

However, as the pumping strength increases further above the threshold, the assumption of fast reservoir relaxation is no longer valid. In this regime, the reservoir dynamics become comparable to the condensate timescale and begin to significantly influence the evolution of the instability. It is therefore necessary to analyze the system in the strong-pumping regime, where the reservoir response and the resulting soliton dynamics exhibit qualitatively different behavior. This regime is considered in the following section.

B. Strong-pumping regime

In contrast to the weak-pumping regime discussed above, we now consider the opposite limit of strong pumping characterized by

$$\frac{P_0}{P_{\text{th}}} \gg 1. \quad (50)$$

In this regime, the reservoir density is no longer slaved perturbatively to the condensate density, and its dynamics must be treated more explicitly.

Retaining terms up to first order in the asymptotic expansion parameter λ , the reservoir rate equation (7b) is conveniently expressed in the moving coordinate

$$\zeta = x - \eta(y, t), \quad (51)$$

which follows the transverse deformation of the soliton. Under this coordinate transformation, the time derivative becomes

$$\partial_t m_R^0 = -\eta_t \partial_\zeta m_R^0. \quad (52)$$

Substituting eq.(51) into the reservoir equation yields

$$-\eta_t \frac{\partial m_R^0}{\partial \zeta} + (\gamma_R + R|\psi_s|^2)m_R^0 = \gamma_C(1 - |\psi_s|^2). \quad (53)$$

This provides a first-order ordinary differential equation governing the leading-order reservoir perturbation,

$$\frac{\partial m_R^0}{\partial \zeta} + \frac{\gamma_R + R|\psi_s|^2}{\eta_t} m_R^0 = \frac{\gamma_C(1 - |\psi_s|^2)}{\eta_t}. \quad (54)$$

The corresponding integrating factor is defined as

$$P(\zeta) = \frac{\gamma_R + R|\psi_s|^2}{\eta_t}. \quad (55)$$

Thus, in the strong-pumping regime, the reservoir polaron density responds locally to the condensate wavefunction, but its spatial variation is also modulated by the soliton deformation through the moving coordinate ζ .

IV. NUMERICAL RESULTS

Having examined the dynamics of exciton–polariton condensates in both weak- and strong-pumping regimes using the asymptotic description in the previous section, we now investigate their behavior numerically by solving the dissipative GP equation (7a) coupled with the reservoir rate equation (7b). The condensate dynamics are computed using the split-step Crank–Nicolson method [37–40], while the reservoir evolution is integrated using a fourth-order Runge–Kutta method. In the simulations, the spatial discretization is chosen as $dx = dy = 0.05$, and the time step is $dt = 10^{-4}\pi$.

A. Instability in the absence of pumping

Before analyzing the influence of pumping and reservoir dynamics on the transverse instability, it is useful to first examine the behaviour of the system in the absence of the pumping. In this limit, the condensate evolves without gain or loss mechanisms and the reservoir density is set to zero ($m_R = 0$). Studying this limit allows us to isolate the intrinsic instability mechanism of a two-dimensional dark soliton without the influence of external driving or reservoir-mediated effects.

In a conservative condensate, a planar dark soliton is dynamically unstable against transverse perturbations. Small modulations along the direction parallel to the soliton stripe grow with time through the well-known snake instability. As the instability develops, the initially straight soliton begins to bend and eventually breaks into a sequence of vortex–antivortex pairs. This process represents a fundamental pathway for the generation of quantized vortices from non-topological excitations and plays a central role in the nonlinear dynamics of two-dimensional quantum fluids. Investigating this regime therefore provides an important reference point for understanding the role of higher-order interactions and nonlinear effects in the evolution of the instability. In particular, it allows us to identify the baseline dynamics of the soliton decay and the formation of vortex structures before additional mechanisms such as pumping and reservoir coupling are introduced.

Figure 2 illustrates the dynamics of a dark soliton undergoing snake instability, leading to the emergence of a well-defined vortex necklace. This pattern formation results from the interplay between the initial soliton profile and the repulsive three-body interaction ($\chi = 1$), with the instability seeded by a small modulation amplitude ($A = 0.25$) in the absence of reservoir effects ($m_R = 0$). The temporal density evolution shown in Figs. 2(a)–(c) captures the progressive breakup of the soliton into discrete topological defects, demonstrating the transition from a one-dimensional soliton stripe to a two-dimensional array of vortices driven by the snake instability.

The corresponding phase profiles in Figs. 2(d)–(f) provide clear topological evidence of the emerging vortex states. The characteristic 2π phase windings confirm the presence of quantized vortices. At the same time, the structure in Fig. 2(f) distinctly reveals the formation of a vortex–antivortex pair, a hallmark of topological excitation associated with the decay of dark solitons in confined geometries [13, 15].

Overall, we find that repulsive three-body interactions play a crucial role in determining the instability pathway and the resulting vortex configuration. Rather than producing disordered or turbulent dynamics, the higher-order interactions guide the system towards an organized topological arrangement manifested as a vortex necklace. This underscores the importance of beyond-two-body interactions in dictating nonlinear dynamics and pattern

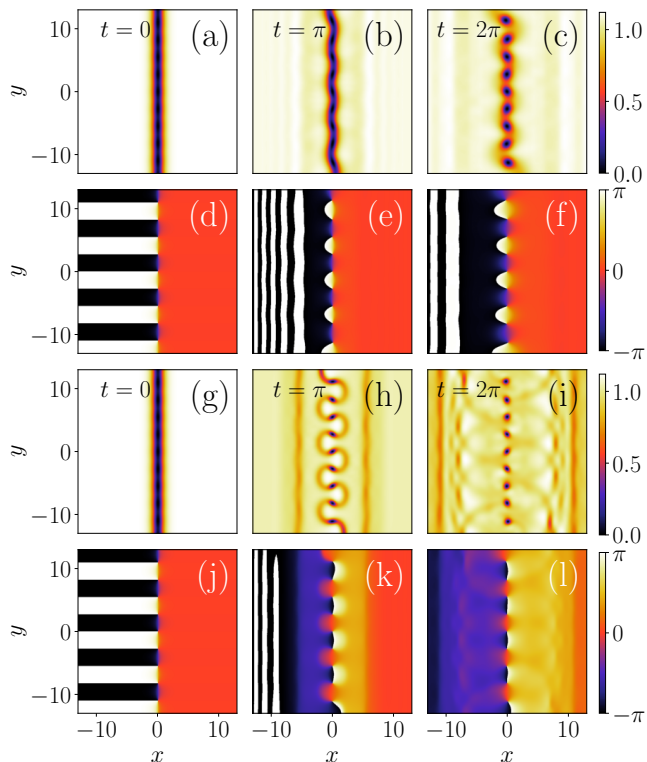


FIG. 2. Evolution of a dark soliton subject to snake instability, leading to the formation of a vortex necklace. The dynamics are driven by repulsive three-body interactions ($\chi = 1$) and an initial modulation amplitude $A = 0.25$, without a reservoir ($m_R = 0$). The top row (a–c) tracks the development of the instability in the density profile, while the bottom row (d–f) shows the associated phase, where the discrete 2π phase jumps and the clear signature of a vortex-antivortex pair in (f) confirm the nature of the topological defects. The dynamics for the attractive three-body interaction ($\chi = -0.2$) and an initial modulation amplitude $A = 0.25$, without reservoir effects (g)–(i) represent the density evolution and (j)–(l) the associated phase profiles.

formation in quantum fluids, and suggests promising avenues for controlled vortex engineering in polariton systems.

B. Weak Pumping

1. Repulsive three-body interaction

In this section, we analyze the impact of repulsive three-body interactions in governing the dynamical stability of a dark soliton in an exciton–polariton condensate. In the weak-pumping regime, binary interactions alone drive vortex formation, with the reservoir density adjusting adiabatically to changes in the condensate density. The introduction of three-body interactions, however, significantly modifies the condensate dynamics, leading to marked changes in the onset and evolution of

snake instability.

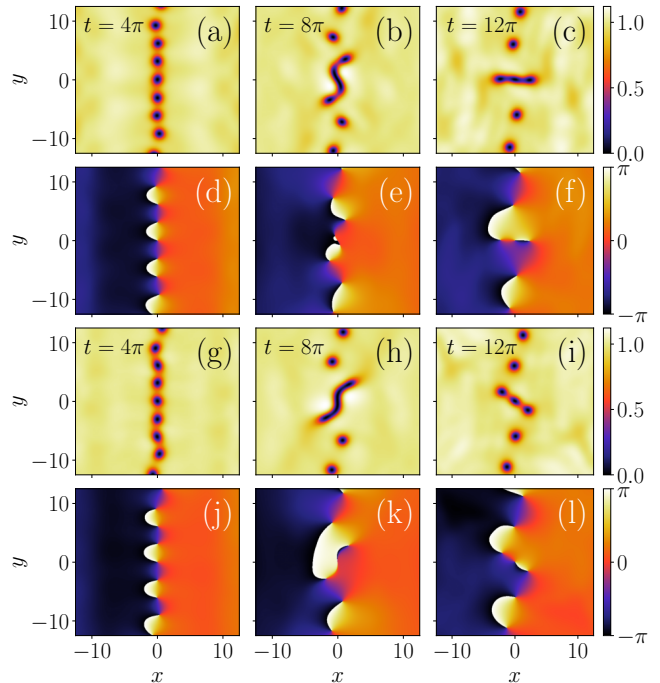


FIG. 3. Comparative evolution of dark solitons undergoing snake instability for two different instability amplitudes in the presence of repulsive three-body interactions ($\chi = 1$) and reservoir coupling. For amplitude $A = 0.25$, (a)–(c) show the density evolution, and (d)–(f) the corresponding phase evolution. For amplitude $A = 0.5$, (g)–(i) present the density evolution, and (j)–(l) the associated phase profiles. In both cases, the wavenumber is $k = 1.0$, and the chemical potential is $\mu = 1$. The density plots illustrate the breakup of the dark soliton into vortex–antivortex pairs, whose lifetimes depend strongly on the initial amplitude. The phase plots reveal characteristic phase windings that confirm vortex formation and show the damping effects induced by reservoir coupling. Other parameters are the same as in Fig. 2.

In Fig. 3 we show the comparative evolution of dark solitons undergoing snake instability for two different instability amplitudes ($A = 0.25$ and $A = 0.5$) in the presence of repulsive three-body interactions ($\chi = 1$) and reservoir coupling. The density profiles shown in Fig. 3 clearly demonstrate that increasing the initial instability amplitude significantly accelerates the breakup of the dark soliton. For the lower amplitude case ($A = 0.25$) [panels (a)–(c)], the soliton exhibits a relatively gradual transverse modulation, leading to a delayed onset of the snake instability and the formation of a limited number of vortex–antivortex pairs. In contrast, for the higher amplitude ($A = 0.5$) [panels (g)–(i)], the instability develops more rapidly, resulting in a pronounced and earlier fragmentation of the soliton. This accelerated decay produces a larger number of vortex–antivortex pairs, indicating an enhanced growth of unstable modes. The subsequent dynamics reveal that these pairs propagate in opposite directions, a characteristic signature of snake

instability, and their increasing density marks the transition from a coherent solitonic structure to a more disordered, turbulent flow regime.

The corresponding phase profiles [Fig. 3(d)–(f) and (j)–(l)] provide further insight into the evolution of the system. In both cases, the phase maps exhibit well-defined 2π phase windings localized at the vortex cores, confirming the formation of topological defects following soliton decay. For $A = 0.25$ [panels (d)–(f)], the phase structure evolves more smoothly, reflecting the slower nucleation and separation of vortex–antivortex pairs. By contrast, for $A = 0.5$ [panels (j)–(l)], the phase becomes increasingly fragmented at earlier times, consistent with the rapid proliferation of vortices observed in the density profiles. Moreover, the phase evolution captures the dissipative influence of the reservoir coupling, which introduces damping into the system. This effect manifests as a gradual smoothing of phase gradients and modifies both the trajectories and lifetimes of the vortex pairs. Consequently, the interplay between nonlinear interactions and reservoir-induced dissipation governs not only the onset of instability but also the subsequent dynamics and persistence of the emergent vortex–antivortex structures.

As illustrated in Fig. 4, increasing the reservoir-induced damping accelerates the disintegration of vortex–antivortex pairs, thereby enhancing the turbulent nature of the polariton fluid. In contrast to Fig. 3, where vortex pairs persist for longer times and propagate more coherently, the present regime exhibits shorter vortex lifetimes along with a more pronounced loss of phase coherence. This behavior suggests that stronger reservoir coupling not only hastens the decay of individual vortices but also suppresses their long-range dynamical evolution.

Furthermore, from Eq. (48), we can see that the lifetime of the vortex necklace depends on γ_C , γ_R , and A . Consequently, in Fig. 4, the polariton lifetime remains unaffected by variations in the chemical potential.

Notably, the region over which the snake instability develops remains spatially narrow in Fig. 4, similar to the behavior observed in Fig. 3. This suggests that the soliton bending and subsequent vortex shedding continue to occur in a localized manner, despite the enhanced dissipation. However, unlike the previous case, the emitted vortex–antivortex pairs here undergo faster annihilation and fragmentation, leading to a more disordered and strongly damped turbulent regime.

To investigate vortex stability in the repulsive regime, we analyze the snake instability of dark solitons including reservoir effects. As shown in Fig. 5, a clear snake instability occurs without interference from boundary effects, indicating that dark solitons can undergo this instability while supporting stable vortices.

For weak pumping ($R = 1$, $A = 0.5$), the characteristic lifetime τ is eight times the reference time τ_0 [panels (a)–(c)]. Increasing the reservoir scattering rate reduces the timescale, resulting in stable vortex formation: for $R = 5$, τ_1 is five times smaller [panels (d)–(f)], and for

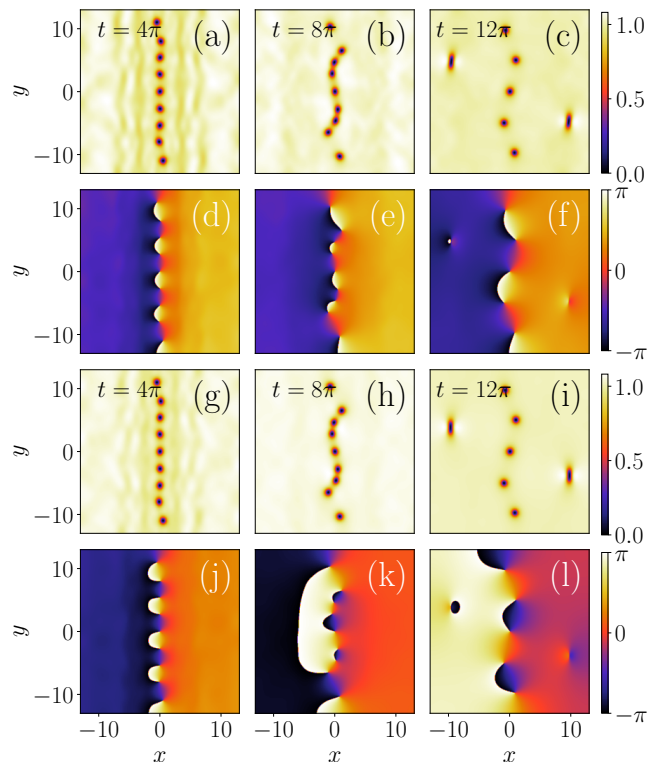


FIG. 4. Comparative evolution of dark solitons undergoing snake instability for different initial amplitudes in the presence of repulsive three-body interactions ($\chi = 1$) and reservoir coupling. The top two rows correspond to an initial amplitude $A = 0.25$: panels (a)–(c) show the density evolution, while (d)–(f) display the corresponding phase profiles. The bottom two rows present the results for $A = 0.5$: panels (g)–(i) depict the density evolution, and (j)–(l) show the associated phase profiles. In both cases, the wavenumber is $k = 1.0$, and the chemical potential is $\mu = 1$. The remaining parameters are fixed as $g_R = 2$, $\gamma_C = 3$, $\gamma_R = 15$, and $R = 0.5$.

$R = 10$, it becomes ten times smaller [panels (g)–(i)], with minimal boundary effects. This demonstrates that higher scattering stabilizes vortex necklaces by suppressing boundary-induced disruptions.

Next, we consider the role of attractive three-body interactions on the dynamical instability of the exciton–polariton condensate.

2. Attractive three-body interaction

We now investigate the effect of attractive three-body interactions ($\chi < 0$) on the dynamical stability of dark solitons under weak pumping. This scenario contrasts with the repulsive case and highlights how the sign of the three-body nonlinearity governs vortex formation and persistence.

In Fig. 6, we illustrate the condensate dynamics in the presence of an attractive three-body interaction ($\chi = -0.2$) combined with repulsive binary interactions, for a

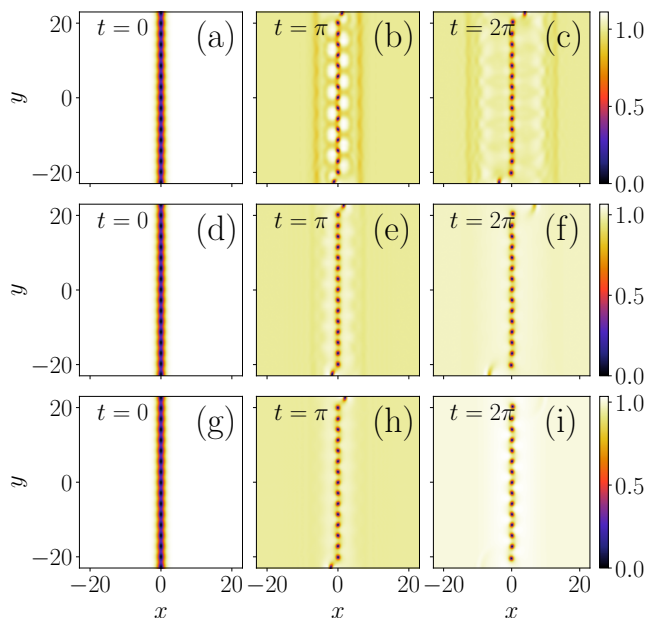


FIG. 5. Time evolution of density profiles illustrating the snake instability of a dark soliton with repulsive three-body interactions, shown for an initial perturbation amplitude $A = 0.5$ and weak pumping conditions. Panels (a)–(i) illustrate vortex formation influenced by the reservoir at different stimulated scattering rates: (a)–(c) $R = 1$, (d)–(f) $R = 5$, and (g)–(i) $R = 10$. Other parameters are fixed at $g_R = 2$, $\gamma_R = 3$, and $\gamma_C = 15$.

fixed instability amplitude of $A = 0.25$. We observe that, although vortices are initially nucleated along the dark soliton, they fail to maintain coherent structures over time. Specifically, the vortex necklace, or string of vortices, that forms is inherently unstable and gradually dissipates, in stark contrast to the repulsive three-body interaction case, where stable vortex configurations are observed. This instability manifests as a rapid breakdown of the vortex arrangement, leading to a highly transient and less structured flow within the condensate. The attractive interaction thus introduces a strong tendency toward decay, preventing the formation of long-lived topological defects.

Increasing the instability amplitude further amplifies this effect, as shown in Fig. 7. The number of unstable vortices grows with larger amplitudes, reflecting the enhanced susceptibility of the system to dynamical instability under attractive three-body interactions. Unlike the repulsive regime, where each pronounced bending of the dark soliton typically results in a single stable vortex, the attractive interaction produces multiple vortices per instability cycle. However, these vortices remain short-lived and fail to establish persistent structures, leading to an increasingly disordered and chaotic vortex pattern. In the weak-pumping regime, the vortex lifetime is governed by γ_C , γ_R , and the instability amplitude A , in agreement with Eq. (48) and the numerical results. While the spe-

cific interactions determine the detailed dynamics, the asymptotic analysis clearly shows how τ_0 depends on the system parameters that set the polariton lifetime.

Another remarkable consequence of the attractive three-body interaction is the widening of the snake instability along the soliton trajectory. While the repulsive case confines the instability to a relatively narrow region, the attractive interaction induces a larger spatial deformation of the soliton. This broadening facilitates the nucleation of a greater number of vortex–antivortex pairs, but their inherent instability ensures that the resulting structures are highly transient. Overall, the attractive three-body interaction enhances both the amplitude and spatial extent of the soliton’s bending, promoting a more turbulent and irregular condensate dynamics compared to the repulsive interaction regime.

C. Strong Pumping

1. Repulsive three-body interaction

For strong pumping, we observe a complete distortion of the snake instability, as shown in Fig. 9. Unlike the repulsive domain, where the snake instability results in the stable formation of a vortex necklace, the attractive three-body interaction leads to a more pronounced and rapid breakdown of the vortex structure. This results in a chaotic and less stable configuration of vortices, with the instability further distorting the soliton profile. The complete distortion of the instability under strong pumping contrasts sharply with the behavior seen in the repulsive regime, where vortex structures remain relatively stable.

Overall, we find that the attractive interaction leads to greater instability, faster breakdown of vortex structures, and more complex, transient vortex patterns compared to the repulsive case.

In contrast, in the attractive domain, the snake instability is influenced by boundary effects, which play a crucial role in disrupting the stability of the vortex configurations, as shown in Fig. 8. At a low scattering rate with $R = 1$ [panels (a–c)], the system exhibits a relatively slow evolution of the dark soliton. The initial configuration shows the emergence of a dark soliton in an unstable state, with slight distortions appearing due to the attractive interactions [panel (a)]. As time progresses [panel (b)], the condensate exhibits the formation of small, localized vortices at the edges of the soliton, which are initially stable. At later times, some of these vortices begin to coalesce, signaling the early stage of vortex instability driven by boundary effects. Despite the relatively weak interaction with the reservoir, the instability in the attractive regime begins to manifest through small oscillations and structural changes in the vortex patterns.

At a moderate scattering rate of $R = 5$ [panels (d–f)], boundary effects become more pronounced, and the dynamics exhibit a more rapid transition towards instability. As shown in panel (d), the initial soliton con-

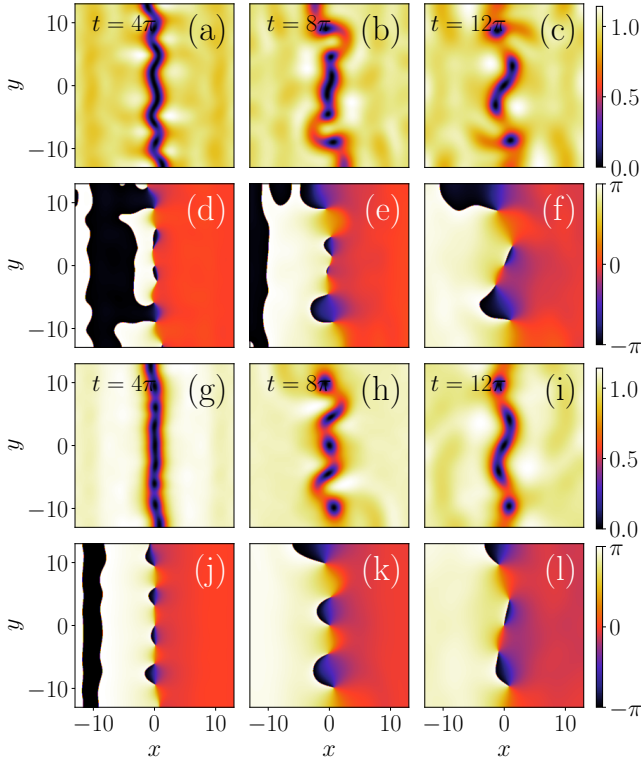


FIG. 6. Comparative evolution of dark solitons undergoing snake instability for different chemical potentials in the presence of the attractive three-body interactions ($\chi = -0.2$) and the reservoir coupling. The top two rows correspond to an initial chemical potential of $\mu = 0.25$: panels (a)-(c) show the density evolution, while (d)-(f) display the corresponding phase profiles. The bottom two rows present the results for $\mu = 0.5$: panels (g)-(i) depict the density evolution, and (j)-(l) show the associated phase profiles. In both cases, the wave number is $k = 1.0$, and the instability amplitude is $A = 0.25$. The remaining parameters are fixed as $g_R = 2$, $\gamma_C = 3$, $\gamma_R = 15$ and $R = 0.5$.

figuration remains identifiable, though vortex formation becomes increasingly chaotic, with the soliton becoming distorted due to enhanced scattering. The vortices that form at the soliton boundaries move and interact more vigorously, and boundary effects accelerate their destabilization [panel (e)]. The system exhibits clear signs of turbulence, as vortices rapidly decay and become disrupted by reservoir interactions. Eventually, the vortices break down completely, and the soliton loses its stability [panel (f)].

At the highest scattering rate of $R = 10$, the system undergoes even more drastic destabilization. The soliton becomes significantly deformed and fragmented, as shown in panel (g). As time progresses, the vortices become highly mobile, rapidly moving and colliding with one another as they fragment [panel (h)], ultimately driving the system into a strongly unstable state where boundary effects overwhelm the vortex structures. Further, the vortices almost get completely dissolved, and

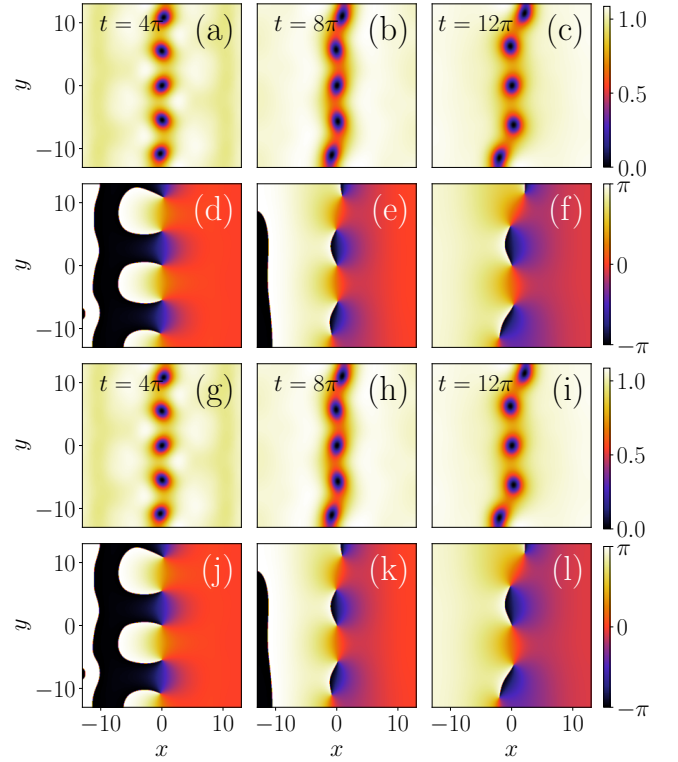


FIG. 7. Comparative evolution of dark solitons undergoing snake instability for different chemical potentials in the presence of the attractive three-body interactions ($\chi = -0.2$) and the reservoir coupling. The top two rows correspond to an initial amplitude of $\mu = 0.25$: panels (a)-(c) show the density evolution, while (d)-(f) display the corresponding phase profiles. The bottom two rows present the results for $\mu = 0.5$: panels (g)-(i) depict the density evolution, and (j)-(l) show the associated phase profiles. In both cases, the wave number is $k = 0.5$, and the instability amplitude is $A = 0.5$. The remaining parameters are fixed as $g_R = 2$, $\gamma_C = 3$, $\gamma_R = 15$ and $R = 0.5$.

the soliton no longer exhibits any coherent structure, reflecting the destructive influence of both the high scattering rate and the boundary effects in this attractive regime [see panel (i)].

Overall, we find that in contrast to the repulsive domain, where vortex structures tend to remain stable, the attractive regime is marked by a rapid destabilization of the vortices. This instability is heavily influenced by boundary effects, which arise due to the competition between attractive interactions and coupling to the reservoir. As the scattering rate increases, the vortices are progressively destabilized, eventually breaking down and disappearing.

Having discussed the impact of the repulsive three-body interaction on the vortex instability mechanism in the exciton-polariton condensate, we now shift our focus to analyze the effects of the attractive three-body interaction on the system's dynamics. The introduction of attractive interactions fundamentally alters the balance

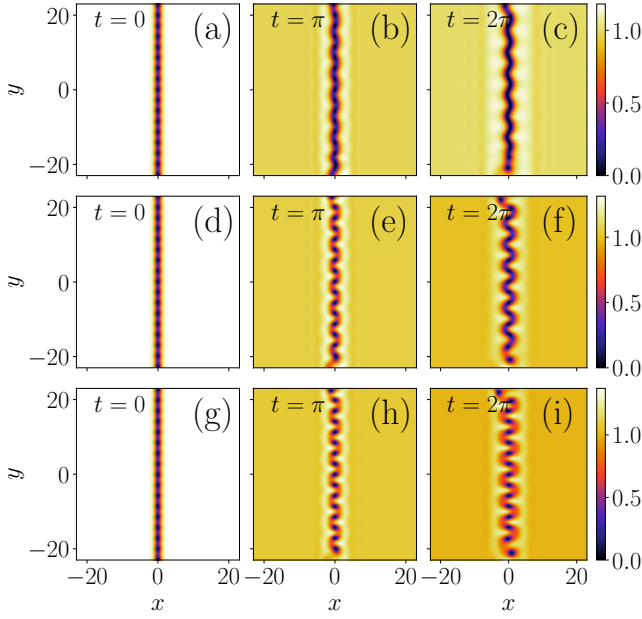


FIG. 8. Time evolution of density profiles illustrating the snake instability of a dark soliton under attractive three-body interactions, shown for an initial perturbation amplitude $A = 0.5$ and weak pumping conditions. Panels (a)–(i) illustrate vortex formation influenced by the reservoir at different stimulated scattering rates: (a)–(c) $R = 1$, (d)–(f) $R = 5$, and (g)–(i) $R = 10$. Other parameters are fixed at $g_R = 2$, $\gamma_R = 3$, and $\gamma_C = 15$.

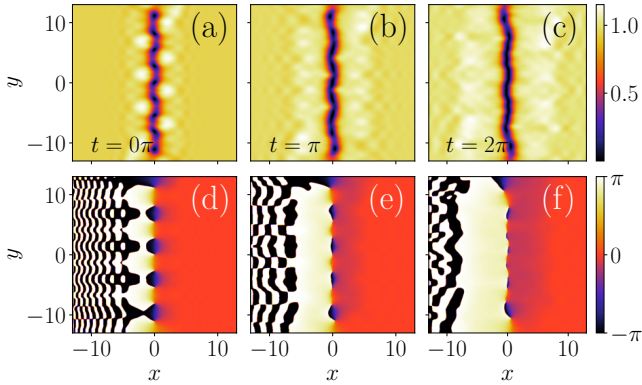


FIG. 9. Vortex creation of dark soliton with attractive three-body interaction for different chemical potentials of $\mu = 1.0$. The $R = 0.08$, $A = 1.0$. In the attractive case with perturbation, it prevents the formation of the vortices. Parameters are $g_R = 2$, $\gamma_C = 0.0075$, $\gamma_R = 0.07$. Under the attractive interaction, the inhomogeneous background destroys the vortex necklace (a)–(c).

of forces within the condensate, potentially leading to different instability mechanisms, vortex dynamics, and flow behaviors compared to the repulsive case.

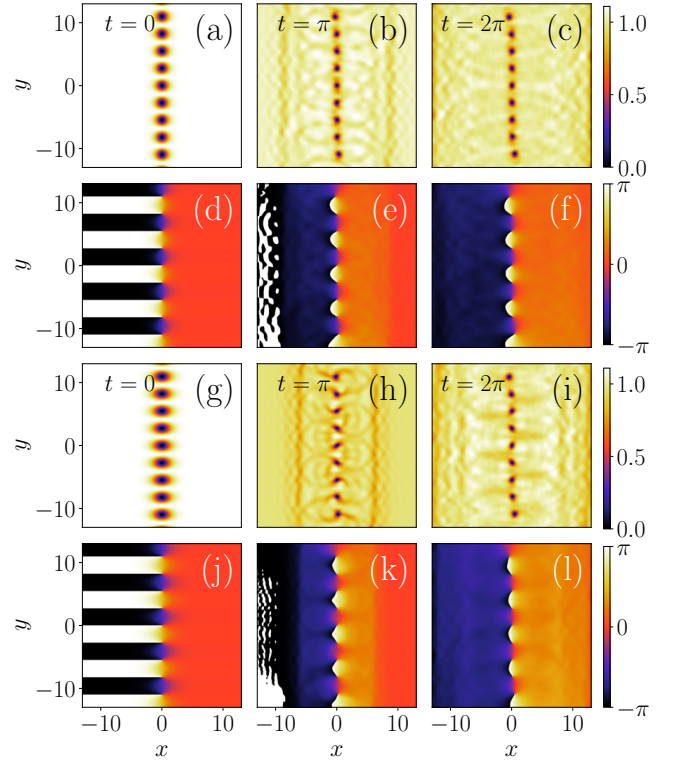


FIG. 10. Evolution of a dark soliton undergoing snake instability in the presence of repulsive three-body interactions ($\chi = 1$) and reservoir coupling. The initial instability amplitude is $A = 1.0$, and the scattering rate is $R = 0.5$. Panels (a)–(c) show the development of vortices leading to snake instability, and panels (d)–(f) show the corresponding phases. This evolution ultimately results in the breakdown of the condensate due to strong reservoir pumping at $\mu = 0.5$. Panels (g)–(i) show the vortex dynamics for a higher pump strength, $\mu = 1.0$, while the corresponding phases are shown in panels (j)–(l). Other parameters are $g_R = 2$, $\gamma_C = 0.0075$, and $\gamma_R = 0.07$.

2. Attractive three-body interaction

In the strong-pumping regime, at a higher instability amplitude of $A = 1.0$, the system supports the formation of a stable vortex necklace, as shown in Fig. 10. Unlike the transient vortex–antivortex pairs observed at lower amplitudes, the vortex necklace constitutes a highly structured and robust configuration. These results highlight the intricate interplay between pumping strength, three-body interactions, reservoir-induced damping, and instability amplitude in determining vortex stability in exciton–polariton condensates. The non-local coupling between the reservoir and the condensate polaritons ensures the persistence of the vortex over a full cycle, in agreement with the asymptotic description under strong pumping for both repulsive and attractive three-body interactions, as discussed in Sec. III B.

V. SUMMARY AND CONCLUSION

In this paper, we have developed a comprehensive study of the dynamics and stability of exciton-polaritons within the framework of the open-dissipative Gross-Pitaevskii equation, incorporating both binary and short-range three-body interactions. Using an asymptotic description, we derived equations for the instability amplitude, offering new insights into vortex formation through the snake instability of dark solitons. Our findings reveal that the interplay between binary and three-body interactions plays a crucial role in the stability and behavior of vortices in these systems.

In particular, we found that a repulsive three-body interaction, when combined with the binary interaction, promotes the formation of a stable vortex-antivortex pair. These pairs exhibit robust dynamics for a longer period, indicating the stability of the vortices for the repulsive regime. In contrast, the introduction of attractive three-body interactions exacerbates the snake instability, leading to a rapid vortex disintegration driven by boundary effects. These boundary effects, influenced by the coupling to the reservoir, are found to destabilize vortices more efficiently in the attractive regime, underscoring the destructive influence of the boundary-induced perturbations.

The time evolution of the instability, influenced by reservoir effects, further highlights the pronounced contrast between the repulsive and attractive three-body interaction regimes. In particular, the vortices in the repulsive regime remain stable for longer periods, whereas in the attractive regime, the vortices are prone to more rapid destabilization due to the stronger boundary ef-

fects. The varying width and number of vortices observed in different scenarios are governed by the nature of the three-body interactions and the parameters of the exciton-polariton system, providing a clearer understanding of the role of these interactions in vortex formation and dynamics.

A detailed formalism of the vortex dynamics for exciton-polariton condensates with three-body interactions will be helpful for future experiments in the system. In this work, we considered the system in the weak-pumping regime, where reservoir effects play a significant role. A natural next step would be to extend the analysis to more strongly pumped systems, where the dynamics of the condensate might be dominated by non-equilibrium phenomena such as superfluid turbulence or pattern formation. Studying these regimes could reveal richer dynamical behavior and provide a deeper understanding of the interplay between dissipation, noise, and nonlinear interactions in open quantum systems. The study of vortex-antivortex annihilation or the formation of non-trivial topological defects in the presence of attractive or repulsive interactions could offer novel insights into topological quantum fluids and the effects of dissipation on topological order.

ACKNOWLEDGMENTS

RR wishes to acknowledge financial assistance received from DST-CURIE (DST-CURIE/PG/54/2022) and ANRF (DST-CRG/008153/2023) in the form of sponsored research projects. The work of P.M. is supported by the Ministry of Education, Rashtriya Uchchatar Shiksha Abhiyan (MoE RUSA 2.0): Bharathidasan University – Physical Sciences.

-
- [1] J. Kasprzak, M. Richard, S. Kundermann, A. Baas, P. Jeambrun, J. M. J. Keeling, F. M. Marchetti, M. Szymańska, R. André, J. a. Staehli, *et al.*, Bose-einstein condensation of exciton polaritons, *Nature* **443**, 409 (2006).
 - [2] R. Balili, V. Hartwell, D. Snoke, L. Pfeiffer, and K. West, Bose-einstein condensation of microcavity polaritons in a trap, *Science* **316**, 1007 (2007).
 - [3] H. Deng, H. Haug, and Y. Yamamoto, Exciton-polariton Bose-Einstein condensation, *Rev. Mod. Phys.* **82**, 1489 (2010).
 - [4] M. Aßmann, J.-S. Tempel, F. Veit, M. Bayer, A. Rahimi-Iman, A. Löffler, S. Höfling, S. Reitzenstein, L. Worschech, and A. Forchel, From polariton condensates to highly photonic quantum degenerate states of bosonic matter, *Proc. Natl. Acad. Sci.* **108**, 1804 (2011).
 - [5] M. Caldara, O. Bleu, F. M. Marchetti, J. Levinsen, and M. M. Parish, Quantum droplets of light in semiconductor microcavities, *Phys. Rev. Lett.* **136**, 116902 (2026).
 - [6] W. Bao, X. Liu, F. Xue, F. Zheng, R. Tao, S. Wang, Y. Xia, M. Zhao, J. Kim, S. Yang, *et al.*, Observation of Rydberg exciton polaritons and their condensate in a perovskite cavity, *Proc. Natl. Acad. Sci.* **116**, 20274 (2019).
 - [7] T. Byrnes, N. Y. Kim, and Y. Yamamoto, Exciton-polariton condensates, *Nature Physics* **10**, 803 (2014).
 - [8] K. Peng, W. Li, M. Sun, J. D. H. Rivero, C. Ti, X. Han, L. Ge, L. Yang, X. Zhang, and W. Bao, Topological valley hall polariton condensation, *Nat. Nanotechnol.* **19**, 1283 (2024).
 - [9] I. Carusotto and C. Ciuti, Quantum fluids of light, *Rev. Mod. Phys.* **85**, 299 (2013).
 - [10] S. Sabari, R. K. Kumar, R. Radha, and P. Muruganandam, Stability window of trapless polariton Bose-Einstein condensates, *Phys. Rev. B* **105**, 224315 (2022).
 - [11] K. Choo, O. Bleu, J. Levinsen, and M. M. Parish, Polaronic polariton quasiparticles in a dark excitonic medium, *Phys. Rev. B* **109**, 195432 (2024).
 - [12] M. Wouters and I. Carusotto, Excitations in a nonequilibrium Bose-Einstein condensate of exciton polaritons, *Phys. Rev. Lett.* **99**, 140402 (2007).
 - [13] J. Keeling and N. G. Berloff, Spontaneous rotating vortex lattices in a pumped decaying condensate, *Phys. Rev. Lett.* **100**, 250401 (2008).
 - [14] A. Amo, J. Lefrère, S. Pigeon, C. Adrados, C. Ciuti, I. Carusotto, R. Houdré, E. Giacobino, and A. Bramati,

- Superfluidity of polaritons in semiconductor microcavities, *Nat. Phys.* **5**, 805 (2009).
- [15] K. G. Lagoudakis, M. Wouters, M. Richard, A. Baas, I. Carusotto, R. André, L. S. Dang, and B. Deveaud-Plédran, Quantized vortices in an exciton–polariton condensate, *Nat. Phys.* **4**, 706 (2008).
- [16] L. Dominici, G. Dagvadorj, J. M. Fellows, D. Ballarini, M. De Giorgi, F. M. Marchetti, B. Piccirillo, L. Marrucci, A. Bramati, G. Gigli, *et al.*, Vortex and half-vortex dynamics in a nonlinear spinor quantum fluid, *Sci. Adv.* **1**, e1500807 (2015).
- [17] H. Flayac, I. A. Shelykh, D. D. Solnyshkov, and G. Malpuech, Topological stability of the half-vortices in spinor exciton-polariton condensates, *Phys. Rev. B* **81**, 045318 (2010).
- [18] S. Christopoulos, G. B. H. von Högersthal, A. J. D. Grundy, P. G. Lagoudakis, A. V. Kavokin, J. J. Baumberg, G. Christmann, R. Butté, E. Feltin, J.-F. Carlin, *et al.*, Room-temperature polariton lasing in semiconductor microcavities, *Phys. Rev. Lett.* **98**, 126405 (2007).
- [19] A. Amo, T. C. H. Liew, C. Adrados, R. Houdré, E. Giacobino, A. V. Kavokin, and A. Bramati, Exciton–polariton spin switches, *Nat. Photonics* **4**, 361 (2010).
- [20] M. Sich, D. N. Krizhanovskii, M. S. Skolnick, A. V. Gorbach, R. Hartley, D. V. Skryabin, E. A. Cerda-Méndez, K. Biermann, R. Hey, and P. V. Santos, Observation of bright polariton solitons in a semiconductor microcavity, *Nat. Photonics* **6**, 50 (2011).
- [21] O. A. Egorov, D. V. Skryabin, A. V. Yulin, and F. Lederer, Bright cavity polariton solitons, *Phys. Rev. Lett.* **102**, 153904 (2009).
- [22] L. A. Smirnov, D. A. Smirnova, E. A. Ostrovskaya, and Y. S. Kivshar, Dynamics and stability of dark solitons in exciton-polariton condensates, *Phys. Rev. B* **89**, 235310 (2014).
- [23] J. Levinsen, F. M. Marchetti, J. Keeling, and M. M. Parish, Spectroscopic signatures of quantum many-body correlations in polariton microcavities, *Phys. Rev. Lett.* **123**, 266401 (2019).
- [24] J. Levinsen, M. M. Parish, and G. M. Bruun, Impurity in a Bose-Einstein condensate and the efimov effect, *Phys. Rev. Lett.* **115**, 125302 (2015).
- [25] A. Hammond, L. Lavoine, and T. Bourdel, Tunable three-body interactions in driven two-component Bose-Einstein condensates, *Phys. Rev. Lett.* **128**, 083401 (2022).
- [26] J. B. Sudharsan, R. Radha, and P. Muruganandam, Collisionally inhomogeneous Bose–Einstein condensates with binary and three-body interactions in a bichromatic optical lattice, *J. Phys. B: At. Mol. Opt. Phys.* **46**, 155302 (2013).
- [27] V. Ramesh Kumar, R. Radha, and M. Wadati, Phase engineering and solitons of Bose–Einstein condensates with two- and three-body interactions, *J. Phys. Soc. Japan* **79**, 074005 (2010).
- [28] R. Sasireka, O. T. Lekeufack, A. Uthayakumar, and S. Sabari, Stability analysis of 3D cubic-quintic Gross–Pitaevskii equation with elastic and inelastic collisions, *AIP Adv.* **15**, 045208 (2025).
- [29] E. A. Ostrovskaya, J. Abdullaev, M. D. Fraser, A. S. Desyatnikov, and Y. S. Kivshar, Self-localization of polariton condensates in periodic potentials, *Phys. Rev. Lett.* **110**, 170407 (2013).
- [30] J. Kasprzak, M. Richard, S. Kundermann, A. Baas, P. Jeambrun, J. M. J. Keeling, F. M. Marchetti, M. H. Szymańska, R. André, J. L. Staehli, *et al.*, Bose–Einstein condensation of exciton polaritons, *Nature* **443**, 409 (2006).
- [31] D. Bajoni, P. Senellart, E. Wertz, I. Sagnes, A. Miard, A. Lemaître, and J. Bloch, Polariton laser using single micropillar GaAs-GaAlAs semiconductor cavities, *Phys. Rev. Lett.* **100**, 047401 (2008).
- [32] A. L. Fetter and A. A. Svidzinsky, Vortices in a trapped dilute Bose-Einstein condensate, *J. Phys. Condens. Matter* **13**, R135 (2001).
- [33] M. R. Matthews, B. P. Anderson, P. C. Haljan, D. S. Hall, C. E. Wieman, and E. A. Cornell, Vortices in a Bose-Einstein condensate, *Phys. Rev. Lett.* **83**, 2498 (1999).
- [34] A. Aftalion, *Vortices in Bose-Einstein Condensates* (Birkhäuser Boston, 2006).
- [35] A. C. White, B. P. Anderson, and V. S. Bagnato, Vortices and turbulence in trapped atomic condensates, *Proc. Natl. Acad. Sci.* **111**, 4719 (2014).
- [36] L. A. Smirnov and V. A. Mironov, Dynamics of two-dimensional dark quasisolitons in a smoothly inhomogeneous Bose-Einstein condensate, *Phys. Rev. A* **85**, 053620 (2012).
- [37] P. Muruganandam and S. Adhikari, Fortran programs for the time-dependent Gross–Pitaevskii equation in a fully anisotropic trap, *Comput. Phys. Commun.* **180**, 1888 (2009).
- [38] D. Vudragović, I. Vidanović, A. Balaž, P. Muruganandam, and S. K. Adhikari, C programs for solving the time-dependent Gross–Pitaevskii equation in a fully anisotropic trap, *Comput. Phys. Commun.* **183**, 2021 (2012).
- [39] R. K. Kumar, L. E. Young-S., D. Vudragović, A. Balaž, P. Muruganandam, and S. Adhikari, Fortran and C programs for the time-dependent dipolar Gross–Pitaevskii equation in an anisotropic trap, *Comput. Phys. Commun.* **195**, 117 (2015).
- [40] R. Ravisankar, D. Vudragović, P. Muruganandam, A. Balaž, and S. K. Adhikari, Spin-1 spin-orbit- and Rabi-coupled Bose–Einstein condensate solver, *Comput. Phys. Commun.* **259**, 107657 (2021).

Appendix A: Derivation of ∇S

The current density of the wavefunction for $\hbar = 1$ and $M = 1$ is given by;

$$\vec{j}(\vec{r}, t) = \frac{1}{2i} [\Psi^* \nabla \Psi - (\nabla \Psi^*) \Psi]. \quad (\text{A1})$$

The current density can also be written as

$$\vec{j}(\vec{r}, t) = n \vec{v}(\vec{r}, t), \quad (\text{A2})$$

where $n = n_0^C$. Hence, ∇S becomes

$$\nabla S = \frac{1}{2i} \frac{[\Psi^* \nabla \Psi - (\nabla \Psi^*) \Psi]}{n}. \quad (\text{A3})$$

This can be written as

$$\nabla S = \frac{\mathbf{Im}(\Psi^* \nabla \Psi)}{|\Psi|^2}, \quad (\text{A4})$$

$$v_x = \frac{\mathbf{Im}(f^* \partial_x f)}{|f|^2}, \quad v_y = \frac{\mathbf{Im}(f^* \partial_y f)}{|f|^2}. \quad (\text{A5})$$

The wavefunction is defined as

$$\Psi = \sqrt{n}(\tanh u + iA(t)\operatorname{sech} u \sin ky) \quad (\text{A6})$$

Here, $f = \tanh u + iA(t)\operatorname{sech} u \sin ky$. The derivatives can be written as,

$$\frac{\partial f}{\partial u} = \operatorname{sech}^2 u - iA \operatorname{sech} u \tanh u \sin ky \quad (\text{A7a})$$

$$\frac{\partial f}{\partial y} = ikA(t) \cos ky \operatorname{sech} u \quad (\text{A7b})$$

$$|f|^2 = A(t)^2 \sin^2(ky) \operatorname{sech}^2(u) + \tanh^2(u) \quad (\text{A7c})$$

In $|f|^2$, the instability amplitude is $A(t) \ll 1$. Then $A(t)^2 \sin^2(ky) \approx 1$

$$v_x = \frac{\mathbf{Im}(f^* \partial_x f)}{|f|^2}, v_y = \frac{\mathbf{Im}(f^* \partial_y f)}{|f|^2} \quad (\text{A7d})$$

$$v_x = -A(t) \operatorname{sech}^3 u \sin ky - \tanh^2(u) \operatorname{sech} u \sin ky \quad (\text{A7e})$$

$$v_y = -A(t) \tanh(u) \operatorname{sech} u \cos ky, \quad (\text{A7f})$$

where $u = x/\xi$. The equations will now become

$$v_x = -A(t) \operatorname{sech}^3\left(\frac{x}{\xi}\right) \sin ky - \tanh^2\left(\frac{x}{\xi}\right) \operatorname{sech}\left(\frac{x}{\xi}\right) \sin ky \quad (\text{A7g})$$

$$v_y = -A(t) \tanh\left(\frac{x}{\xi}\right) \operatorname{sech}\left(\frac{x}{\xi}\right) \cos ky \quad (\text{A7h})$$